



## OPEN Lithospheric features revealed by a new Moho map in the central-western Sicily Channel

Simona Bongiovanni<sup>1✉</sup>, Mariagiada Maiorana<sup>1</sup>, Antonino D'Alessandro<sup>2</sup>, Raffaele Martorana<sup>1</sup> & Attilio Sulli<sup>1</sup>

A detailed Moho map is essential for understanding the deep structure of a given area, especially for a complex area such as the Sicily Channel, shaped by the Europa-Africa convergence. We built a new Moho map of the central-western Sicily Channel using a multidisciplinary approach, which comprises the analysis of crustal seismic reflection profiles and velocity models from multiple databases. We found two earthquake alignments that occurred in the study area from 1981 to the present that reach sub-Moho depths and through which we constructed two lithospheric seismogenic volumes (LSVs). We then related these results with the location of the volcanoes, the tectonic structures, and the rheological profiles present in the literature. This work aims to expand the limited knowledge of the geodynamic setting and lithospheric structure of the Sicily Channel. Furthermore, it can constitute a starting point for future works regarding the seismic hazard of the area.

**Keywords** Moho depth, Sicily Channel, Lithospheric seismogenic volume, Seismic reflection profiles

The Sicily Channel is a seismically active area, characterized by moderate seismicity with a magnitude generally below 5. Unfortunately, the location of the earthquakes hypocenters in this area is poorly constrained because due to the sparse distribution of permanent seismic stations and the high attenuation<sup>1</sup>.

As illustrated in Fig. 1a, an alignment of earthquakes with sinistral strike-slip focal mechanisms occurs in the western sector of the Sicily Channel as noted by several authors<sup>2–5</sup>.

The Sicily Channel hosts eight seismogenic sources (Fig. 1b): four with approximately N-S trends in the western sector and near the Sicilian coast (Fig. 1b within the blue dashed line) and four with N-S trends crossing the Grabens (Fig. 1b within the red dashed line). These are mapped in the DISS (Database of Individual Seismogenic Sources)<sup>6</sup>.

The Sicily Channel has been greatly influenced by the interaction between Africa and Europe plates. Among the various deformation stages recorded, the most important one began in the Late Miocene with the formation of the Sicilian Fold and Thrust Belt (SFTB)<sup>7</sup>. In the Pliocene, an NNE-SSW-oriented extensional mechanism produced the Graben of Malta, Linosa and Pantelleria<sup>8–10</sup>; at the same time, the Gela Thrust System (GTS) emplacement occurred<sup>11</sup> as well as the formation of a N-S oriented left strike-slip mechanism<sup>12</sup>, that extends from Capo Granitola-Sciacca to Linosa (CGSFZ)<sup>5,9</sup> (Fig. 1c). The latter, physically separating the Graben of Pantelleria from those of Malta and Linosa (Fig. 1c), induced a different evolution between them; the earthquakes available in the area confirm that this structure is currently active and involves the lithosphere levels<sup>9,13</sup>. Along this deformation belt, also a relevant magmatic activity is recorded, which was associated with the formation of magmatic manifestations, constituting several volcanoes and volcanic banks (Fig. 1a), scattered in the whole Sicily Channel<sup>13–16</sup>. Near the coast of western Sicily, volcanic edifices of the Quaternary age were discovered by Lodolo et al.<sup>17</sup>. According to Civile et al.<sup>5</sup>, in this system, the magma rises through the faults, acting as conduits, that cut across the entire lithosphere leading to a partial melting by decompression. The seismic section CROP M23 (location in Fig. 1a) of Catalano et al.<sup>18</sup> highlighted the deep structural layers of this highly deformed zone, revealing a mild Moho rising from west to east of the CGSFZ tectonic structure, and a Moho deepening beneath the Gela Thrust System. Civile et al.<sup>19</sup> also detected in the seismic line CROP M25 (location in Fig. 1a) a Moho rising under the Pantelleria Graben, probably linked to deep fluids rising causing several volcanic manifestations around Pantelleria Island (Fig. 1c). This interpretation is supported by the gravity model realized along the seismic profile showing a Moho rising to about 17 km, in the NW of Pantelleria Graben, and, to the N and S of the Pantelleria Graben, a Moho deepening at 24–25 km depth<sup>19</sup>.

<sup>1</sup>Dipartimento di Scienze della Terra e del Mare, Università di Palermo, Palermo, Italy. <sup>2</sup>Istituto Nazionale di Geofisica e Vulcanologia, Osservatorio Nazionale Terremoti, Rome, Italy. ✉email: simona.bongiovanni@unipa.it

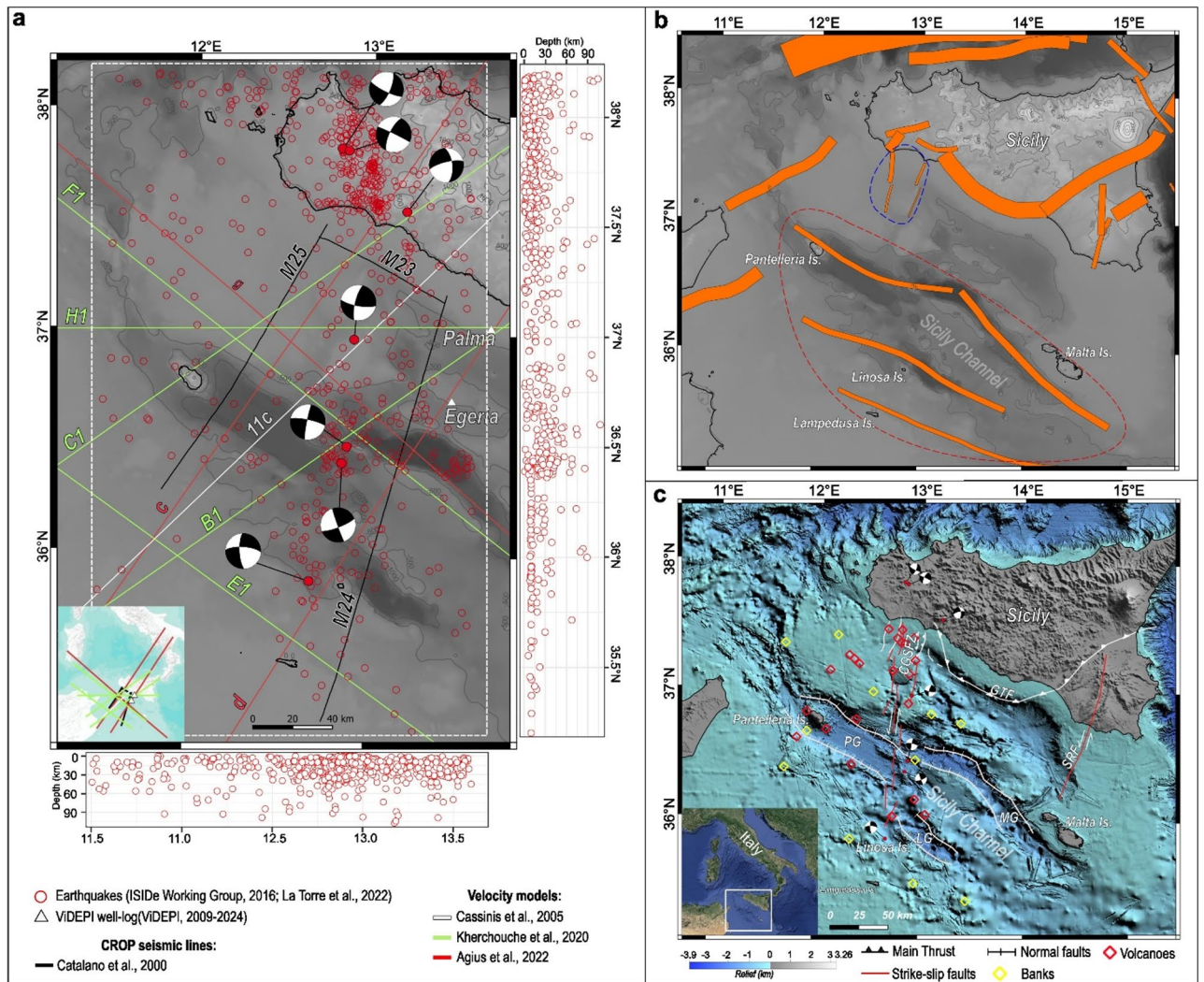


**Fig. 1.** (a) Location of the dataset available for the study area. Focal mechanisms of the major events present in the time domain moment tensor (TDMT) database are also reported<sup>53</sup>; (b) The seismogenic sources detected in the DISS (Database of Individual Seismogenic Source)<sup>6</sup> are shown in orange. The red and blue dashed lines contain the seismogenic sources located in the Sicily Channel; (c) Geological and morpho-structural map of the study area. GTF (Gela Thrust Front)<sup>54</sup>, LG (Linosa Graben), MG (Malta Graben), PG (Pantelleria Graben), CGSFZ (Capo Granitola-Sciaccà fault zone)<sup>5</sup>, SRF (Scicli-Ragusa Fault)<sup>5</sup>. Focal mechanisms of the major events present in the Time Domain Moment Tensor (TDMT) database are also reported<sup>53</sup>. The location of banks and volcanoes is derived from Aïssi et al.<sup>15</sup> and Lodolo, et al.<sup>17</sup>. Maps generated using QGIS software version 3.30 (<https://download.qgis.org/downloads/>). Hypocenter projections on the horizontal and vertical planes were generated using R software version 4.3.1 and Inkscape version 1.3. DEM used in the maps is from EMODnet (<https://emodnet.ec.europa.eu/geoviewer/#>).

Knowledge of the Moho depth is crucial to gaining insights into the dynamics of the Earth's interior, the evaluation of geohazard, the reconstruction of the lithospheric pattern of a given area and the knowledge of deep structures. The Moho presents different characteristics and geometries depending on whether it lies in oceanic or continental region or is located in areas subjected to extensive or compressive processes<sup>20</sup>.

The Moho is generally determined by means of seismic and/or gravimetric methods.

In the literature, many maps of Moho have been produced by different methods. Suhadolc & Panza<sup>21</sup> and Du et al.<sup>22</sup> generated a map of European Moho obtained from interpretations of CSS (Controlled Source Seismology) profiles.

Moho depth maps have also been created for other regions such as southern California<sup>23</sup>, northern and northeastern China<sup>24–27</sup>, eastern Tibet<sup>28–30</sup> and southern China<sup>31</sup>, using receiver function (RF) analysis. Teng et al.<sup>32</sup> and Reddy & Rao<sup>33</sup> discussed and reviewed refraction seismic profiles for Moho determination in China and reflection seismic profiles for Indian shield Moho determination, respectively. Stankiewicz & De Wit<sup>34</sup> modeled the Moho below South Africa using reflection seismic profiles and RF analysis. These studies emphasize that obtaining reliable depths by using the RF method requires very accurate S-wave and P-wave velocities.

Consequently, reliable results depend on velocity variations with depth, which are best constrained by seismic refraction data.

Mjelde et al.<sup>35</sup> and Aitken et al.<sup>36</sup> determined the Moho depth for South America and Australia, respectively, using gravity data from satellite observation. In addition, Aitken et al.<sup>36</sup> show a limitation of gravity inversion for crustal modeling. These authors noted the unreliability of the method, for example in areas with thick and dense crust or thin and low-density crust, adding that in such a case the method can be made reliable by defining the structure through seismic methods.

Other authors have created Moho maps by integrating data from various methods to overcome the limitations of individual techniques and to ensure better areal coverage. Grad et al.<sup>37</sup> made a Moho map of Europe using seismic and gravity data; Assumpção et al.<sup>38</sup> discussed crustal thickness models of South Africa using data extrapolated from seismic tomography, reflection seismic profiles and receiver function; Tugume et al.<sup>39</sup> made crustal thickness map in Africa and Arabia by interpolating gravity data, RF data and surface wave dispersion.

Regarding the Central Mediterranean area and the Italian region, Nicolich & Dal Piaz<sup>40</sup> and Scarascia et al.<sup>41</sup> produced a Moho isobath map using CSS profiles; Waldhauser et al.<sup>42</sup> and Lippitsch et al.<sup>43</sup>, produced a detailed Moho map of the Alpine region using a method proposed by Waldhauser<sup>44</sup> and Waldhauser et al.<sup>42</sup> to determine 3-D P-wave velocity models; Pontevivo & Panza<sup>45</sup> used surface wave scattering to reconstruct the lithosphere-asthenosphere system of Italy; Lombardi et al.<sup>46</sup> and Piana Agostinetti & Amato<sup>47</sup> proposed a Moho map applying the RF method for the Italian peninsula and the central-western Alps, respectively; Di Stefano et al.<sup>48</sup> and Spada et al.<sup>49</sup> show a Moho map for the Italian peninsula using both CSS and RF data.

However, these maps either partially or completely exclude the Sicily Channel, which lies on the periphery of these models and is poorly detailed. This is primarily because they are mainly produced on a seismological basis and the seismic network in the area is not adequately distributed because stations are located only on land.

Kherchouche et al.<sup>50</sup> proposed a Moho map for the Sicily Channel using ambient noise and earthquake tomography method, but the nearly constant value of about 30 km depth is incompatible with the geological structures in the area.

Jongsma et al.<sup>51</sup>, Agius et al.<sup>1</sup>, and Calò & Parisi<sup>2</sup> report information for this area through the study of earthquakes; Civile et al.<sup>8,19</sup>, Corti et al.<sup>52</sup>, and Palano et al.<sup>13</sup> describe the area focusing on the analysis of the superficial part of seismic reflection profiles.

As a result, the lithospheric knowledge of the Sicily Channel remains incomplete.

With the present work, we want to contribute to the knowledge of the deepest part of the Sicily Channel, specifically in an area where there are several banks and volcanoes, and to provide an instrument that can be used to understand the mechanisms influencing the variation in crustal thickness found in the study area and the possible connection between rising deep magmatic fluids and outcropping volcanoes.

To do this, we used joint analysis of multidisciplinary data. Specifically, we interpreted reprocessed ultra-high penetration seismic reflection profiles<sup>18</sup> calibrated with well-log data to observe detailed surface geometries down to Moho depth and used them to calibrate, in turn, P-wave velocity ( $V_p$ ) and shear wave ( $V_s$ ) models extrapolated from the literature. Further, to understand the connection with structures in the area we merged the seismological contribution using earthquakes with a statistical approach, using the Gaussian Kernel function. The location of this data is shown in (Fig. 1a).

## Results

### Seismo-stratigraphic interpretation

We interpreted CROP seismic profiles M23, M24, and M25 to determine the thickness and the geometries of the main units and structures. On each seismic line, we projected  $V_p$  profiles from Cassinis et al.<sup>55</sup> and Agius et al.<sup>56</sup>. Key reflectors, limiting the main layers from Moho to the seabed, have been identified based on their amplitude, lateral continuity, and velocity variation. The correlation with well data (Egeria and Palma) (location in Fig. 1a) and literature data<sup>5,18,57,58</sup> allowed us to characterize the shallower levels and attribute them to the respective age and feature. The deep layers were identified based on seismic reflection characteristics and velocity variation (Fig. 2).

From the seabed to the horizon corresponding to the Top of Miocene a wide Plio-Pleistocene sedimentary filling is observed; its maximum thickness (1.8 s/TWT) is reached in front of the GTS wedge (Fig. 2a). The reflectors show medium amplitude, high frequency, and parallel geometry, with onlap termination on the GTS and CGSFZ. This unit is composed of pelagic marls and marly limestones of the Zanclean Trubi Fm., and of the Piacenzian-Pleistocene shelf clayey deposits with sandy intercalations of the Ribera Fm.<sup>5,9</sup>

In the northern sector of the study area, the GTS chaotic reflectors, dissected by different S-vergent thrust faults, exceeding 2 s/TWT of thickness, are observed (Fig. 2a).

Underneath this unit, the Miocene deposits are present, consisting of shelf siliciclastic deposits of the Terravecchia Fm. and evaporitic sediments of the Messinian Gessoso-Solfifera Group<sup>5,9</sup>. The seismic signal is characterized by a high amplitude reflector, and medium frequency, with locally transparent zones (Fig. 2a).

Underlying these, the Mesozoic carbonates are observed; these are composed of: the Upper Triassic (Siccia Fm.) and Lower Jurassic (Inici Fm.) deposits consisting of a carbonate platform succession overlain by Jurassic-Eocene pelagic limestones with marly and clayey intercalations (Buccheri, Chiaramonte, Hybla and Amerillo Fms.). Horizons show high lateral continuity, medium frequency, and a sub-parallel configuration (Fig. 2a).

Volcanic manifestations are widespread in the entire study area (Fig. 1a), and volcanic intrusions are visible in all the analyzed seismic lines (Fig. 2a,b). Those are characterized by wide diffraction hyperbolae zones and chaotic facies, sometimes reaching the seafloor.

The deep layers include the units occurring below 5 s/TWT. The crystalline basement is the top of the upper crust, the shallowest of the deep layers, and is identified by a discontinuous and strong reflector lying at an

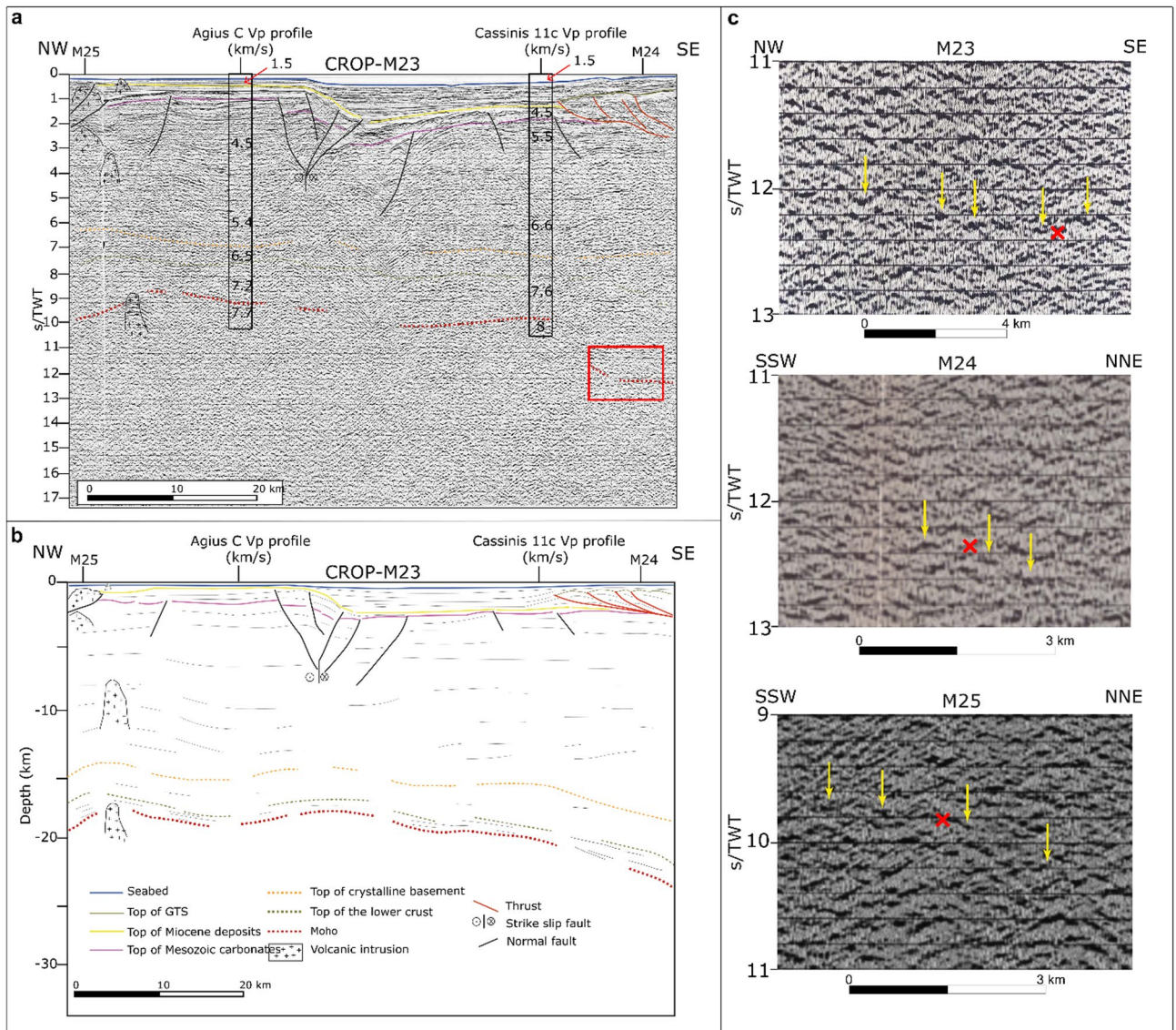


**Fig. 2.** (a) M23 seismic line interpretation after Catalano et al.<sup>18</sup> in time (TWT). The red rectangle corresponds to the close-up shown in c); (b) Line drawing in depth (km). Crossing Vp profiles by Cassinis et al.<sup>55</sup> and Agius et al.<sup>56</sup> have been represented; c - Moho reflection characteristics (indicated by yellow arrows) in M23, M24 and M25 CROP profiles. The red cross in the close-up of line M23 corresponds to the intersection with the Moho recognized in line M24, those in the close-ups of lines M24 and M25 correspond to the intersection with the Moho recognized in line M23.

average depth of 6 s/TWT (10 km) in all the study area<sup>18</sup> and by a Vp velocity variation that goes above 6 km/s at it (Fig. 2a,b).

The top of the lower crust was identified below this, with numerous horizontal (near flat) and gently dipping reflections characterized by low continuity and medium amplitude, locally interrupted by wide diffraction hyperbolae zones. The velocity here increases to more than 7 km/s up to the Moho (Fig. 2a,b). A double laminated, laterally discontinuous reflector occurs at its base; this, according to Catalano et al.<sup>18</sup> interpretation, is assumed to be the Moho horizon. Above the Moho, high amplitude reflectors are also observed, characterizing a high reflective lower crust, *sensu* Catalano et al.<sup>7</sup>.

In seismic profiles M23, M24 and M25, the signal shows high amplitude, low frequency, and it is locally interrupted by diffraction hyperbolae (Fig. 2). The most prominent double reflection is visible in M24 and M25 (Fig. 2c). In proximity to the assumed Moho, the velocity increases up to 8 km/s.

#### Moho surface in time (S/TWT) and in depth (KM)

From the Vs models of Agius et al.<sup>56</sup> and Kherchouche et al.<sup>50</sup> (location shown in Fig. 1a) we obtained Vp values for the Moho surface, which are respectively 8 km/s and 7.7 km/s.

The velocity models of Kherchouche et al.<sup>50</sup> were not used to construct the Moho surface as they did not align well with the other data used and therefore, we used only the 3 velocity models proposed by Agius et al.<sup>56</sup>.

The obtained Moho surface in time ranges from ~6.7 to ~12.6 s/TWT (see Supplementary Fig. S1 online). The lowest values are found beneath the Pantelleria Graben (6.7 s/TWT): there, the contour lines follow the trend of the tectonic structures, which are normal faults at the rims of the Graben (Fig. 1a). Otherwise, between the Pantelleria Graben and the Linosa Plateau sector, the concavity of the contour lines shows a constant NW trend; and, on the contrary, in the proximity of the GTS and in the southern Linosa Graben, a variation in the concavity of the contour lines is observed (see Supplementary Fig. S1 online).

The Moho surface in depth shows strong lateral variation, with depths ranging from ~16.8 to ~27.2 km (Fig. 3a).

In the Pantelleria Graben, the Moho reaches 16.8 km depth, maintaining a shallower trend than in the surrounding areas. Near the Linosa and Malta rims, it reaches depths of around 20 km (Fig. 3a).

Additionally, a Moho deepening is observed along the M23 profile from west to east. At the point where it intersects the orogenic wedge of the GTS, the Moho reaches ~27 km depth (Fig. 3a Supplementary Fig. S2 online).

The study area has a variable bathymetry that affects the Moho depth map. To get information about the crustal structure, we constructed a crustal thickness map (Fig. 3b). The pattern of the crustal thickness map is similar to that of the Moho map and shows greater thicknesses in the GTS sector (~27 km) and lesser thicknesses at the Pantelleria Graben (~18 km) and near Linosa and Malta rims (~19 km).

### Lithospheric seismogenic volumes (LSVs)

From the statistical analysis of each dataset of earthquakes divided into depth ranges, we obtained density plots on which we calculated gradients (example in Fig. 4) and maximum gradient values. Using the isolines, obtained from the maximum density gradient values for each depth range, we determined two pairs of surfaces perpendicular to each other bordering two LSVs also perpendicular to each other: one with N-S trend (blue scale in Fig. 5) and one with E-W trend (red scale in Fig. 5). For lithospheric seismogenic volume, we mean the seismogenic zone where most earthquakes occur<sup>59</sup> involving the crust and upper mantle. The base of this volume corresponds to the brittle-ductile transition zone and is influenced by different factors including the geodynamics of the study area and the composition and physical state of the rocks<sup>59,60</sup>.

It is observed that the N-S-oriented LSV follows the trend of the tectonic structures located within the CGSFZ. Otherwise, the E-W volume shows a trend concordant with the normal faults bordering the Pantelleria, Malta, and Linosa Grabens.

In Fig. 5, the geometry of the N-S-trending LSV's bounding surfaces is well illustrated to the west and east. The volume extends from the northern coast of Sicily to the island of Linosa for about 240 km and from 5 km to about 60 km depth. In particular, the northernmost sector of the volume is present from a depth of 5 km to about 25 km; from the island of Pantelleria southward, the volume deepens to a depth of 60 km.

To the south of the Sicily coast, the volume decreases vertically and is only present from about 20 km depth to about 35 km depth. The minimum, average and maximum distance between the two surfaces, and thus the minimum, average and maximum value of the volume thickness are 35 km, 48 km and 55 km, respectively. The two surfaces also exhibit concavity facing toward the inside of the volume (Fig. 5b,d). The central sector of the NS-trending LSV perpendicularly intersects the EW-trending LSV (red scale in Fig. 5).

The latter extends from a depth of 50 to 60 km and a length of 100 km. The minimum, average and maximum distance between the two surfaces and thus the minimum, average and maximum volume thickness are 50 km, 70 km and 90 km, respectively. The two surfaces bordering the volume exhibit a concavity facing toward the inside of the volume (Fig. 5a,c).

### Discussion

A new, reliable, high-resolution Moho map of the central-western sector of the Sicily Channel.

We used data from different disciplines, which allowed us to have a greater data coverage than the Moho maps produced for the Italian peninsula that showed a gap in the Sicily Channel due to the poor data coverage due to the use of single-discipline data and techniques<sup>41,43,46–49</sup>.

In addition, the Delaunay triangulation method used, offers the advantage of generating a consistent triangular grid, improving the computational accuracy of the model and preserving the original data set without adding or removing data points.

Considering that this new map covers a smaller study area and was made using a wide dataset, it exhibits a higher resolution comparatively to other Moho maps of the Mediterranean and the Italian peninsula<sup>55,57,61</sup>.

Moreover, the map reveals strong lateral variations (the depth ranges between 16.8 km and 27.2 km, see Fig. 3a) conversely to the map proposed by Kherchouche et al.<sup>50</sup> which shows a constant trend in Moho depth within the Sicily Channel, probably due to a not well-distributed seismic network in the area.

Furthermore, our map exhibits a strong correlation with the tectonic structures found in the literature and shown in Fig. 1c (e.g., Pantelleria, Malta, and Linosa Grabens) and with the location of volcanoes; in fact, a shallower Moho (16.8 km depth) is observed in correspondence with the Capo Granitola-Sciaccà offshore, around the Pantelleria, Lampedusa, and Linosa islands and near the volcanoes (Fig. 6).

The two constructed LSVs, if compared with the other data analyzed, are a fundamental tool for understanding the lithosphere structure variation of the study area. Fundamental evidence is that both the N-S and the E-W LSVs show a concordant trend with both tectonic structures (Fig. 1c) and seismogenic sources from the DISS database (Fig. 1b).

Specifically, these LSVs exhibit (i) a NNE-oriented trend (in agreement with Calò & Parisi<sup>2</sup>; Di Stefano et al.<sup>3</sup>; Spampinato et al.<sup>4</sup>; Civile et al.<sup>5</sup>, which follows the structures of the CGSFZ, interpreted by Civile et al. (2018) as

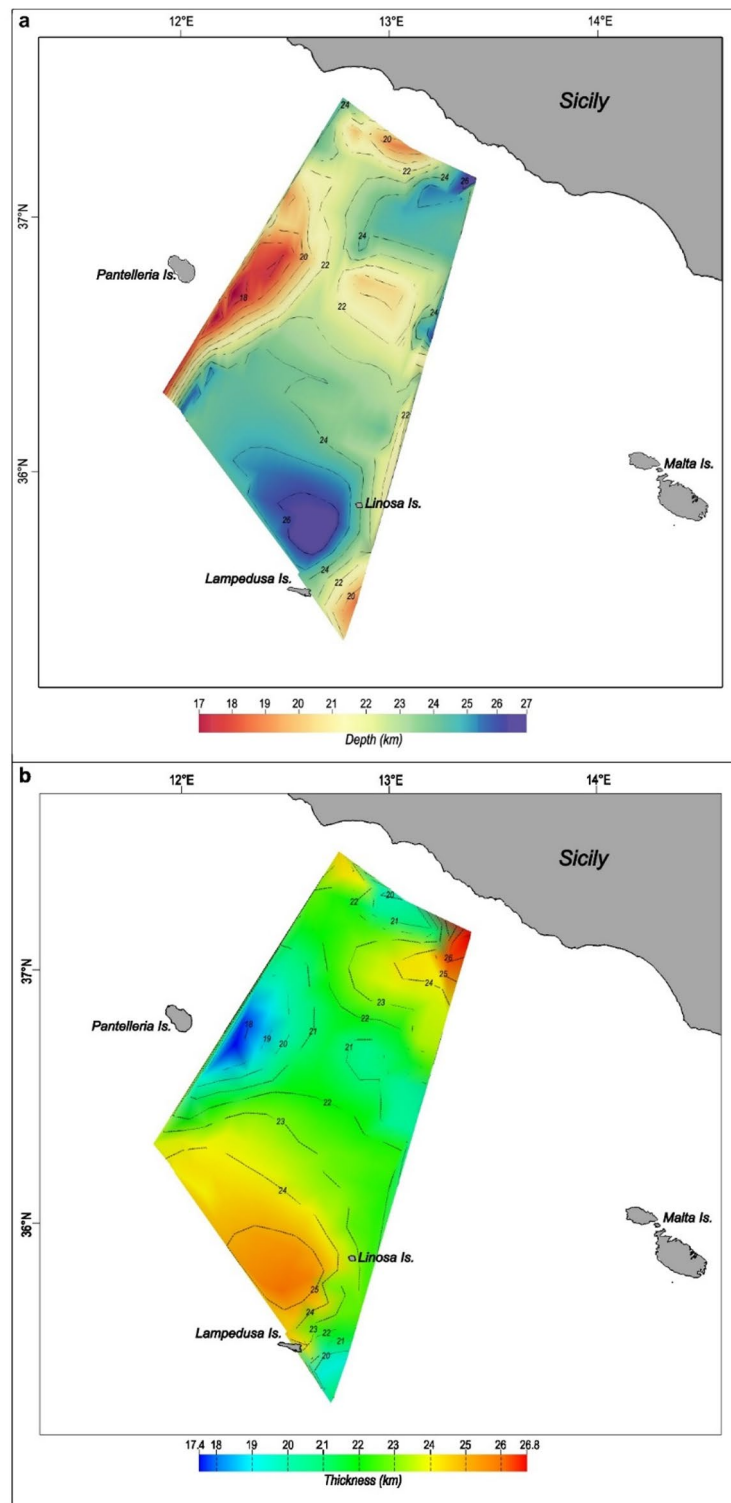


**Fig. 3.** Moho map in depth (a) and the crustal thickness map (b) of the central western sector of the Sicily Channel. Image generated using Move Software version 2022.1 (<https://www.petex.com/pe-geology/move-suite/move/>) and Inkscape version 1.3.

lithospheric faults favoring the rise of magmas to the surface, and (ii) an EW-oriented trend, concordant with the normal faults delineating Pantelleria, Malta, and Linosa Grabens (Fig. 7).

Furthermore, the E-W alignment of seismic events, which has not been widely discussed by other authors, is supported by the presence of an E-W seismogenic source identified in the DISS database.

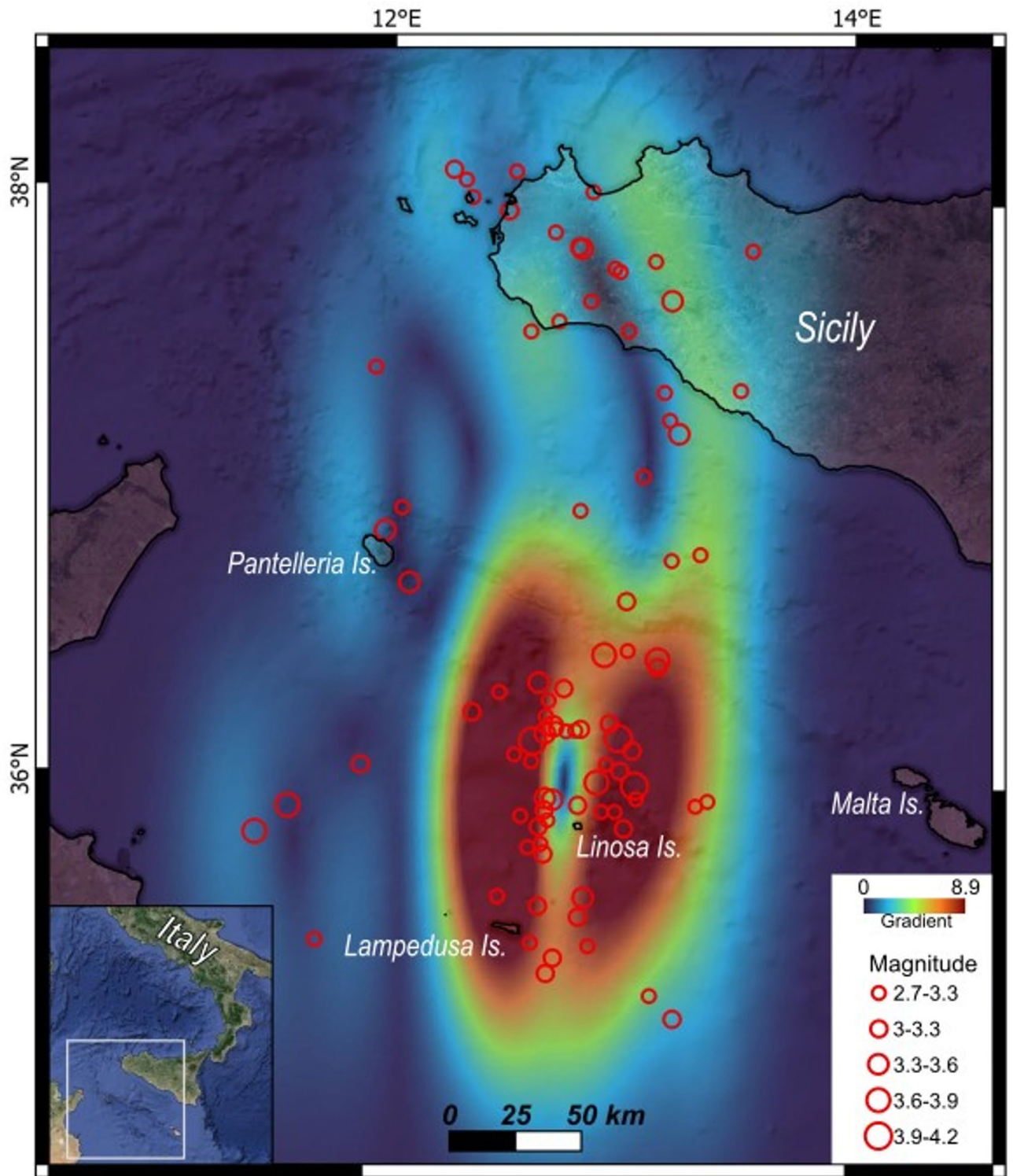


**Fig. 4.** An example of the density gradient (color scale) obtained from the density of earthquakes (red dots) located between 5 and 15 km depth. Image generated using QGIS software version 3.30 (<https://download.qgis.org/downloads/>) and R software version 4.3.1.

In detail, the N-S LSV extends from 5 km to 60 km depth, except in the northernmost region where it lies at a depth between 20 km and 35 km depth (Fig. 5a,c). In this sector, morpho-bathymetric and seismic data from the literature<sup>5,15,17,62</sup> indicate a high concentration of volcanoes, located outside the LSV. Conversely, some volcanoes are observed within the LSV, particularly around Linosa and Pantelleria Islands (Fig. 6). Hence, it is not possible to derive a direct relationship between the location of volcanoes and LSVs.

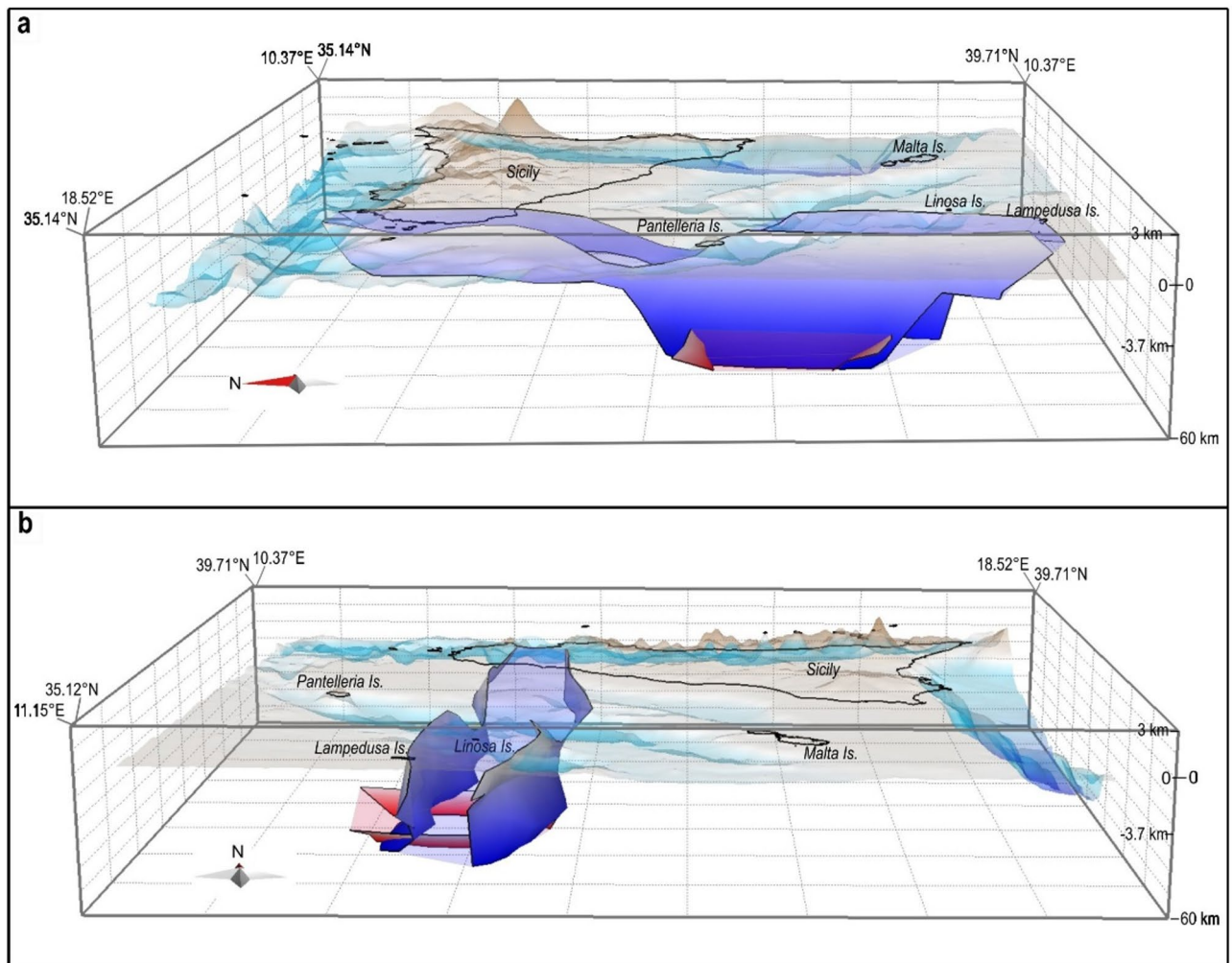


**Fig. 5.** (a–d) Different views of the LSVs represented by the surfaces bordering them laterally. Topography (exaggeration  $\times 8$ ) is represented in blue-brown color scale; in blue scale the LSV with NS trend, in red scale the LSV with EW trend. The fill between the surfaces in transparency represents the volume. Image generated using Move Software version 2022.1 (<https://www.petex.com/pe-geology/move-suite/move/>) and Inkscape version 1.3.

Viti et al.<sup>63</sup> suggest, in the rheological profiles realized for the Sicily Channel, an alternation between viscous and brittle behavior at various depths down to approximately 35 km; down to this value, they observe a predominantly viscous behavior, in agreement with the maximum Moho depth reconstructed in this work (see Fig. 3a).

Analysis of a large earthquake dataset, linked to the reconstruction of a detailed Moho map, has identified sub-moho earthquakes.

Except for subduction zones, the sub-Moho earthquakes in general are rare<sup>64,65</sup>. Otherwise, they are observed in various parts of the world and across different tectonic regimes<sup>66–69</sup>. The two LSVs shown in this paper indicate the presence of seismic events at depths greater than the Moho. Therefore, this is not anomalous as different tectonic regimes coexist in the study area as reported by Calò and Parisi<sup>2</sup>, Corti et al.<sup>52</sup> and Maiorana et al.<sup>10</sup>.

The presence of such sub-Moho events would also suggest the presence of rheological variation in the mantle, but this is not in agreement with the rheological profiles of Viti et al.<sup>63</sup> which give no evidence of brittle behavior under Moho. Therefore, these profiles should be updated.

However, if we consider the absence of a shallow LSV in the north of the Pantelleria volcanic island (Fig. 5a,c) and the absence of it at great depth near to the Linosa volcanic island (Fig. 5b,d), we see that the absence of LSV also gives important information about the mantle rheological nature.

In the first case, the absence of a shallow LSV to the north is in an area where a shallow magma chamber is present, at a depth of about 6 km, also inferred from a significant positive gravimetric anomaly in the complete Bouguer map<sup>17,70</sup>.

In contrast, the absence of a continuous LSV at depth around Linosa is related to the presence of deep magmatic intrusions as indicated by seismic reflection data<sup>10</sup> and to the absence of evolved rocks on Linosa Island indicating a deep magma reservoir<sup>71</sup>.

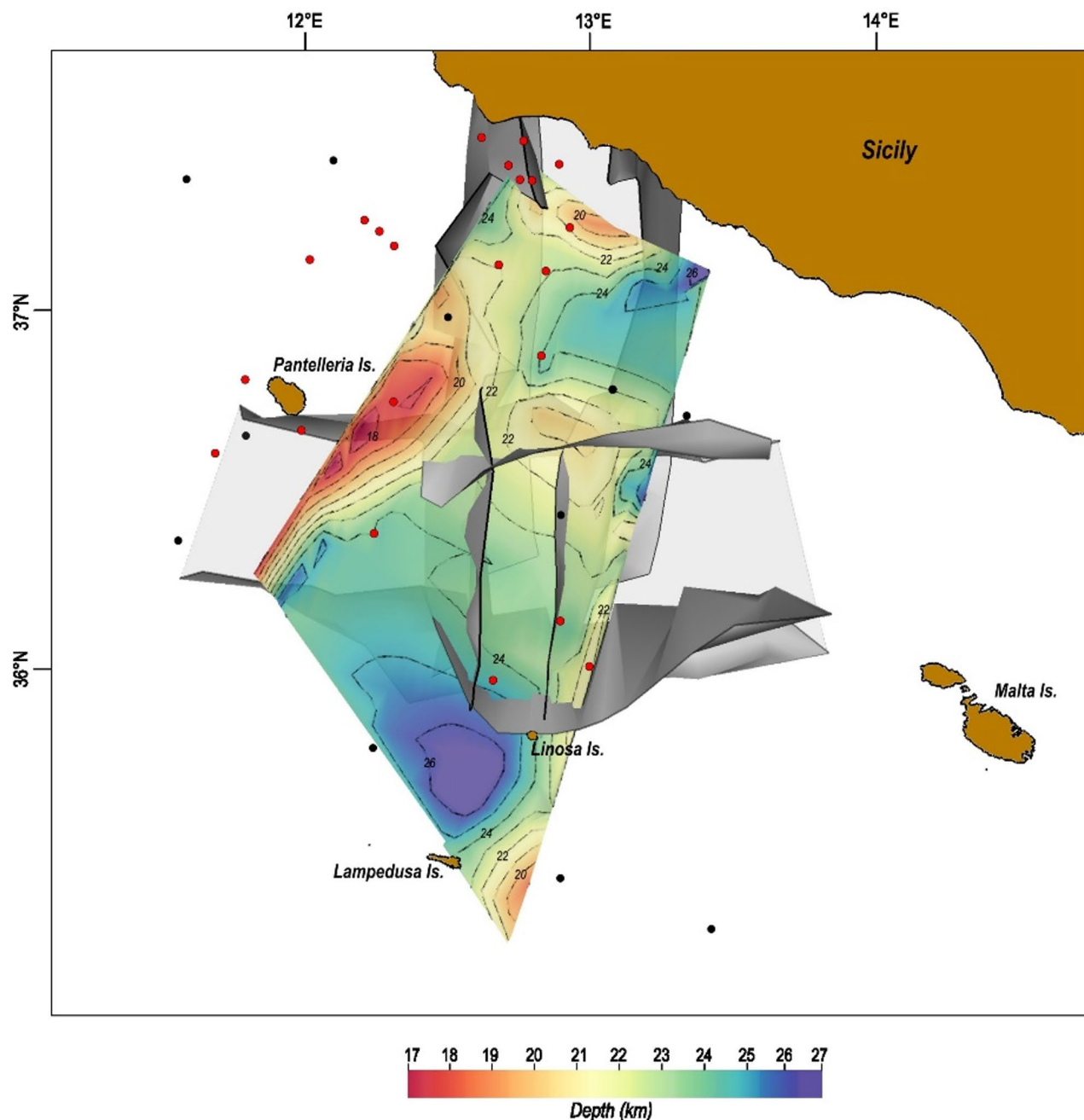


**Fig. 6.** Moho map in depth (color scale) and the LSVs (in grey scale) obtained. The red and black dots represent volcanoes and banks, respectively. Image generated using Move Software version 2022.1 (<https://www.petex.com/pe-geology/move-suite/move/>) and Inkscape version 1.3.

Considering our results, optimizing the localization of earthquakes would be beneficial, thereby improving the accuracy of seismogenic volumes such as those we have produced. Extending the seismic network to include offshore areas could help achieve this goal.

In conclusion, our Moho map of the west-central sector of the Sicilian Channel represents a key tool for constraining to the bottom the crustal velocity models useful for earthquake localization. This is particularly important because, currently, earthquakes in the Sicily Channel are localized using a single velocity model that covers large areas with varying structural characteristics. Moreover, since the E-W trending seismogenic sources extend farther east than the sector we analyzed, it is necessary to extend the analysis to obtain a complete overview of the entire Sicily Channel.

Finally, based on our results, we suggest updating the rheological models proposed in the literature for the Sicily Channel to improve our understanding of the geodynamics and lithospheric structure, which remains still unclear.

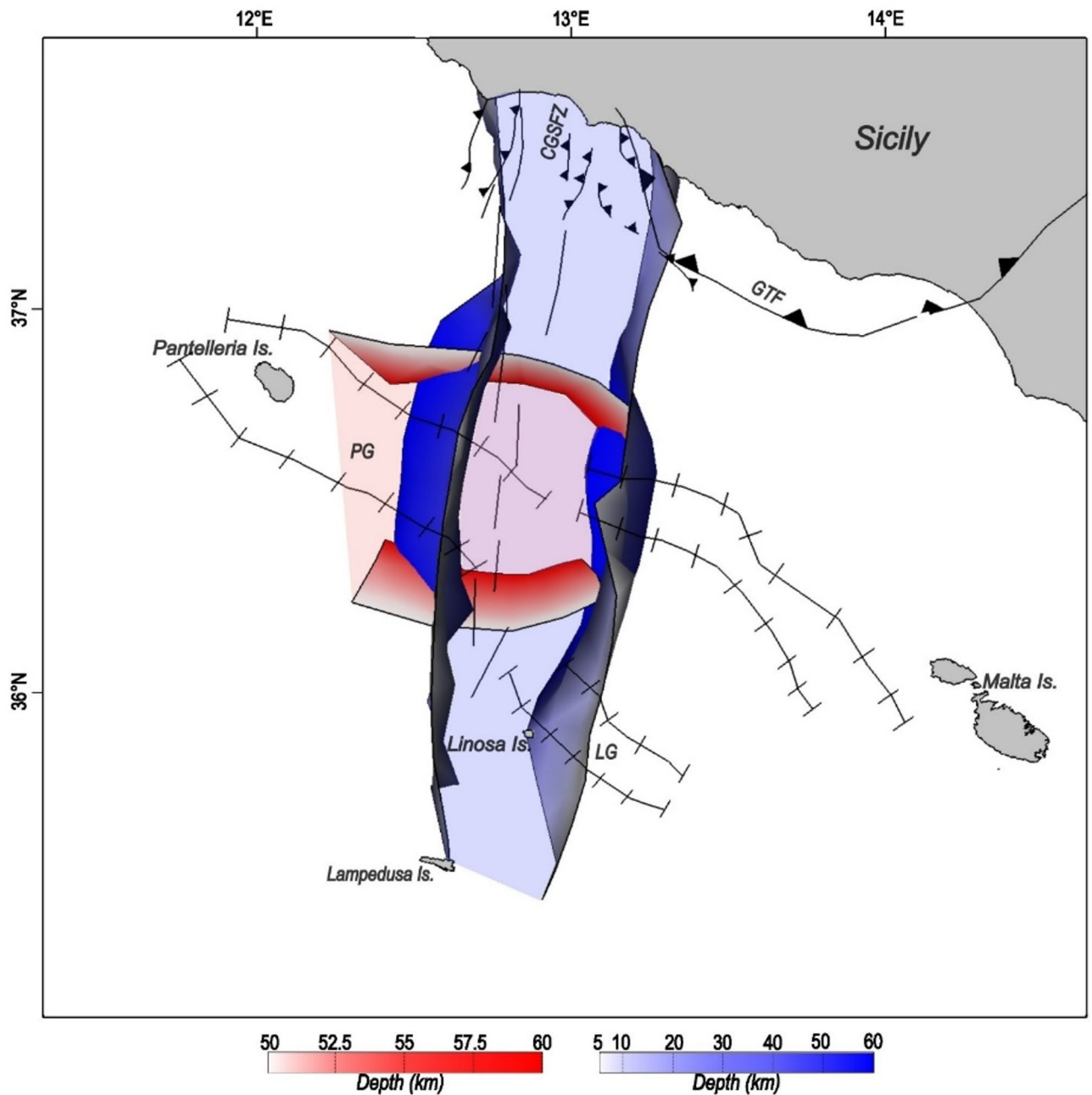


**Fig. 7.** LSVs in plan. LSV with N-S trend, in red scale the LSV with E-W trend. PG (Pantelleria Graben), MG (Malta Graben), LG (Linosa Graben), CGSFZ (Capo Granitola-Sciacca Fault Zone)<sup>5</sup>, GTF (Gela Thrust Front)<sup>54</sup>. Image generated using Move Software version 2022.1 (<https://www.petex.com/pe-geology/move-suite/move/>) and Inkscape version 1.3.

## Methods

### Interpretation of seismic reflection profiles and well-log data

We analyzed intermediate to ultra-high penetration seismic reflection profiles and well-logs data derived from ViDEPI (<https://www.videpi.com/videpi/videpi.asp>) and CROP databases<sup>18</sup> (Fig. 2). The CROP (CROsta Profonda) project (<http://www.crop.cnr.it/>) interpreted the deep crust reflection seismic profiles to map the deepest crustal reflectors. The seismic reflection profiles were acquired in collaboration with CNR-ENI and CNR-ENEL from 1988 to 1995 by the RV OGS-Explora using an Airgun array and a 4500 m long and 180-channel streamer. This represents a multidisciplinary geophysical research project aimed at understanding geodynamic processes, assessing geological hazard, and exploring energy resources in Italy. Approximately 10,000 km of seismic reflection were acquired (about 1250 km on land and about 8700 km at sea). The dataset is publicly available for consultation ([www.videpi.com/videpi/videpi.asp](http://www.videpi.com/videpi/videpi.asp)).

	M23			M24			M25		
	MIN (m/s)	AVE (m/s)	MAX (m/s)	MIN (m/s)	AVE (m/s)	MAX (m/s)	MIN (m/s)	AVE (m/s)	MAX (m/s)
Water	1500	1500	1500	1500	1500	1500	1500	1500	1500
Seabed	1574	1659,57	1887	1615	1983,93	2718	1770	2032,14	1977
GTF	4036	4036	4036	4036	4036	4036	N.A.	N.A.	N.A.
Oligo-Miocene	1160	1851,33	2545	1657	2094,92	2859	1618	2104,93	3290
Meso-Cenozoic	5300	5600	5800	2030	2879,45	3966	1997	2975,91	3951
Upper crust	6000	6000	6000	6000	6000	6000	5788,94	6090,47	6392
Lower crust	6800	7100	7400	7000	7000	7000	7000	7000	7000
Crust/mantle discontinuity	7700	7922,67	8068	8000	8000	8000	8000	8000	8000

**Table 1.** Velocity values obtained for each layer detected in the CROP seismic reflection profiles. Values derive from Sonic logs (Egeria and Palma) analysis, interval velocities tables of the seismic profile, and Vp velocities from Cassinis et al.<sup>55</sup> and Agius et al.<sup>56</sup>.

The interpretation of the dataset was carried out through a seismo-stratigraphic and structural analysis, applying Vail<sup>72</sup>'s method, and implementing a 2.5D geological model using Move Software version 2022.1 (<http://www.petex.com/pe-geology/move-suite/move/>). The interpretation of the seismo-stratigraphic horizons was compared with the analysis of the seismic profiles by various authors<sup>18,73,74</sup>. In the first step the seismic reflection profiles were interpreted on the basis of their reflectivity. Subsequently, intersections with other seismic profiles and velocity profiles were evaluated. The interpretation of the seismo-stratigraphic horizons was compared with the analysis of the seismic profiles by various authors<sup>18,73,74</sup>.

Literature data on the localization of volcanic banks<sup>15,17</sup> were projected on a DEM downloaded from EMODnet (<https://emodnet.ec.europa.eu/geoviewer/#>) (Fig. 1c).

### Velocity data and time to depth conversion

We digitized and analyzed, through the 3D modeling software Move Software version 2022.1 (<https://www.petex.com/pe-geology/move-suite/move/>) which allows 2D data to be visualized in a 3D environment, 5 2D shear velocity models (Vs) obtained from ambient noise and earthquake tomography method by Kherchuche et al.<sup>50</sup>, 3 2D shear velocity models (Vs) inferred from seismic surface waves by Agius et al.<sup>56</sup> and a 2D P-wave velocity model inferred from the WARR (wide-angle reflection-refraction) profiles by Cassinis et al.<sup>55</sup> (Fig. 1a) (see Supplementary Fig. S3 online).

Initially, we converted 2D shear velocity models (Vs) to 2D P-wave velocity models (Vp) using the relationship between Vp and Vs proposed by Menichelli et al.<sup>75</sup> for southern Italy. Since the latter focuses on southern Italy in general and not specifically in off-shore areas, we also used the empirical law proposed by Brocher<sup>76</sup> (see Supplementary Fig. S4.1, S4.2, S4.3 online). The results obtained from the two methods are comparable, so we used the model proposed by Menichelli et al.<sup>75</sup>. Subsequently, we converted these 2D velocity models from depth-to-time through the 3D Time Conversion Tool (see Supplementary Fig. S5 online). In particular, we used the Database method where rock properties, such as the velocity and velocity decay with depth, are assigned to each layer.

We calibrated the P-wave velocity models with seismic reflection profiles. To construct the Moho surface in times (s/TWT), we interpolated- the recognized Moho horizon on each individual profile by Delaunay triangulation method. This method offers the advantage of creating a uniform grid of triangles for better model computation quality, without adding or removing data points from the original dataset. A grid with 4 km x 4 km cells was used for resampling the interpolated surfaces and simplifying it.

For the construction of the Moho surface in depth, we converted velocity models and reflection seismic profiles from time to depth using the 3D Depth Conversion tool and Database method. Velocity values (Table 1) extrapolated from literature<sup>18,41,74</sup> were used to depth-convert the reflection seismic profiles.

We realized a Moho surface in depth (km) with the same method used for the construction of the surface of the Moho in times (s/TWT). In addition, since the depth of the Moho is conditioned by the depth of the seafloor, to provide more information about the crustal structure we constructed the crustal thickness map. The thickness at each point was calculated using the bathymetry as the top and the Moho surface as the bottom.

### Analysis of earthquakes

We considered seismic events from 2005 to 2023 extrapolated from the ISIDe<sup>77</sup> database, which contains the parametric data of all seismic events localized by the INGV. To extend the dataset's temporal range, we also included earthquakes from 1981 to 2018, extrapolated from the CLASS (Catalogo delle Localizzazioni ASSolute) catalog<sup>78</sup>, which contains earthquakes with optimized localizations. For this reason, we removed from the ISIDe catalog those earthquakes with the same ID as the events from 2005 to 2018 in the CLASS catalog (see Supplementary Fig. S6 online for more details regarding seismic events extrapolated from CLASS catalog and associated location errors).

Our research was conducted in the area between latitudes between 35.2° and 38.2° N and longitudes between 11.5° and 13.6° E. The location of epicenters on a horizontal plane and vertical planes of this dataset that we created is shown in (Fig. 1a). The same figure also shows focal mechanisms of the major events, extrapolated from Time Domain Moment Tensor (TDMT) dataset<sup>53</sup>.

At first, we calculated the magnitude of completeness ( $M_c$ ) of the dataset created using the MAXimum Curvature method (MAXC)<sup>79</sup> implemented in the Tremors software-app<sup>80</sup> and we captured STAI (Short-term aftershock incompleteness) periods using the same software-app to avoid overestimation of  $M_c$ .

We implemented a MATLAB code to organize the obtained database of earthquakes into 10-km depth ranges with a 50% overlap. We then analyzed these data through a statistical approach using the R statistical software<sup>81</sup>, a language and environment for statistical processing and graphics.

We implemented a code on R statistical software using a Kernel smoothed intensity function from a point pattern with  $0.01 \times 0.01$ -pixel grid to obtain a density plot of the seismicity for each of these depth ranges.

The intensity estimate has been computed with a *Gaussian* Kernel function and bandwidth chose with the rule of thumb by Scott<sup>82</sup>. The latter determines the width of the window within which the points affecting the calculation of the intensity estimate are located.

In addition, in the computation of density plots, we assigned weights to each seismic event based on magnitude. Specifically, since the energy of an earthquake increases exponentially as the magnitude increases, we assigned an exponentially increasing value for each increasing value of magnitude.

The functions employed here are found in the *raster*<sup>83</sup> and *spatsal*<sup>84</sup> packages of the R statistical software.

For each density plot calculated for each depth range, we obtained the density gradient. Finally, we extrapolated the isolines of the maximum values of the density gradient, interpolated them using the Delaunay triangulation method, and obtained two perpendicular pairs of vertical surfaces bordering two Lithospheric Seismogenic Volumes (LSVs).

## Data availability

The dataset generated and or analyzed in this study are available from the corresponding author, S.B., upon reasonable request.

Received: 4 October 2024; Accepted: 5 May 2025

Published online: 17 May 2025

## References

- Agius, M. R., Galea, P., Farrugia, D. & D'Amico, S. An instrumental earthquake catalogue for the offshore Maltese Islands region, 1995–2014. *Ann. Geophys.* **63** (6), 658. <https://doi.org/10.4401/ag-8383> (2020).
- Calò, M. & Parisi, L. Evidences of a lithospheric fault zone in the Sicily channel continental rift (southern Italy) from instrumental seismicity data. *Geophys. J. Int.* **199** (1), 219–225 (2014).
- Di Stefano, R. et al. A regional-scale discontinuity in Western Sicily revealed by a multidisciplinary approach: A new piece for Understanding the geodynamic puzzle of the Southern mediterranean. *Tectonics* **34** (10), 2067–2085 (2015).
- Spampinato, S. et al. A reappraisal of seismicity and eruptions of Pantelleria Island and the Sicily channel (Italy). *Pure. Appl. Geophys.* **174**, 2475–2493 (2017).
- Civile, D. et al. Capo Granitola-Sciaccia fault zone (Sicilian channel, central Mediterranean): structure vs magmatism. *Mar. Pet. Geol.* **96**, 627–644 (2018).
- DISS Working Group Database of individual seismogenic sources (DISS), version 3.3.0: A compilation of potential sources for earthquakes larger than M 5.5 in Italy and surrounding areas. *Istituto Naz. Di Geofis. E Vulcanologia (INGV)*. <https://doi.org/10.13127/diss3.3.0> (2021).
- Catalano, R. et al. Sicily's fold–thrust belt and slab roll-back: the SI. RI. PRO. Seismic crustal transect. *J. Geol. Soc.* **170** (3), 451–464 (2013).
- Civile, D. et al. The Pantelleria graben (Sicily channel, central Mediterranean): an example of intraplate 'passive'rift. *Tectonophysics* **490** (3–4), 173–183 (2010).
- Civile, D. et al. Morphostructural setting and tectonic evolution of the central part of the Sicilian channel (Central Mediterranean). *Lithosphere* **2021** (1). <https://doi.org/10.2113/2021/7866771> (2021).
- Maiorana, M. et al. Is the Sicily channel a simple rifting zone?? New evidence from seismic analysis with geodynamic implications. *Tectonophysics* **864**, 230019 (2023).
- Di Stefano, E., Infuso, F. & Scarantino, S. Plio-Pleistocene sequence stratigraphy of south western offshore Sicily from well-logs and seismic sections in a high-resolution calcareous plankton biostratigraphic framework. In: Max, M.D., Colantoni, P. (Eds.), *Geological Development of the Sicilian-Tunisian Platform: Unesco Report in Marine Science* **58**, 105–110 (1993).
- Fedorik, J. et al. Structural analysis and Miocene-to-Present tectonic evolution of a lithospheric-scale, transcurrent lineament: the Sciacca fault (Sicilian channel, central mediterranean Sea). *Tectonophysics* **722**, 342–355 (2018).
- Palano, M. et al. Crustal deformation, active tectonics and seismic potential in the Sicily channel (Central Mediterranean), along the Nubia–Eurasia plate boundary. *Sci. Rep.* **10** (1), 21238 (2020).
- Beccaluva, L., Colantoni, P., Di Girolamo, P. & Savelli, C. Upper miocene submarine volcanism in the Strait of Sicily (Banco Senza Nome). *Bull. Volcanol.* **44**, 573–581 (1981).
- Aïssi, M., Rovere, M. & Würtz, M. Sardinia channel—Strait of Sicily—Ionian sea—Adriatic sea seamounts. *Atlas Mediterranean Seamounts Seamount Struct.* (2014).
- Cavallaro, D. & Coltelli, M. The Graham volcanic field offshore Southwestern Sicily (Italy) revealed by high-resolution seafloor mapping and ROV images. *Front. Earth Sci.* **311** (2019).
- Lodolo, E., Zampa, L. & Civile, D. The Graham and terrible volcanic Province (NW Sicilian Channel): gravimetric constraints for the magmatic manifestations. *Bull. Volcanol.* **81**, 1–11 (2019).
- Catalano, R., Franchino, A., Merlini, S. & Sulli, A. A crustal section from the Eastern Algerian basin to the ionian ocean (Central Mediterranean). *Mem. Soc. Geol. It.* **55**, 71–85 (2000).
- Civile, D., Lodolo, E., Tortorici, L., Lanzafame, G. & Brancolini, G. Relationships between magmatism and tectonics in a continental rift: the Pantelleria Island region (Sicily channel, Italy). *Mar. Geol.* **251** (1), 32–46. <https://doi.org/10.1016/j.margeo.2008.01.009> (2008).
- Carbonell, R., Levander, A. & Kind, R. The Mohorovičić discontinuity beneath the continental crust: an overview of seismic constraints. *Tectonophysics* **609**, 353–376 (2013).
- Suhadolc, P. et al. Physical properties of the lithosphere-asthenosphere system in Europe from geophysical data, in *The Lithosphere in Italy*, edited by A. Boriani pp. 15–40, Acad. Naz. dei Lincei, Rome (1989).
- Du, Z., Michelini, A., Panza, G. F. & EurId: A regionalized 3-D seismological model of Europe. *Phys. Earth Planet. Inter.* **106**, 31–62. [https://doi.org/10.1016/S0031-9201\(97\)00107-6](https://doi.org/10.1016/S0031-9201(97)00107-6) (1998).

23. Zhu, L. & Kanamori, H. Moho depth variation in Southern California from teleseismic receiver functions. *J. Geophys. Research: Solid Earth*. **105** (B2), 2969–2980 (2000).
24. Chen, L., Wang, T., Zhao, L. & Zheng, T. Distinct lateral variation of lithosphere thickness in the Northeastern North China craton. *Earth Planet. Sci. Lett.* **267**, 56–68 (2008).
25. Liu, H. & Niu, F. Receiver function study of the crustal structure of Northeast China: seismic evidence for a mantle upwelling beneath the Eastern flank of the Songliao basin and the Changbaishan region. *Earthq. Sci.* **24** (1), 27–33 (2011).
26. He, C. S., Dong, S. W., Chen, X. H., Santosh, M. & Li, Q. S. Crustal structure and continental dynamics of central China: a receiver function study and implications for ultrahigh-pressure metamorphism. *Tectonophysics* **610**, 172–181 (2014).
27. Wang, C. et al. Lateral variation of crustal structure in the Ordos block and surrounding regions, North China, and its tectonic implications. *Earth Planet. Sci. Lett.* **387**, 198–211 (2014).
28. Xu, L., Rondenay, S. & Van der Hilst, R. D. Structure of the crust beneath the southeastern Tibetan plateau from teleseismic receiver functions. *Phys. Earth Planet. Inter.* **165**, 176–193 (2007).
29. Zhang, Z. et al. Crustal structure across Longmenshan fault belt from passive source seismic profiling. *Geophys. Res. Lett.* **36**, L17310. <https://doi.org/10.1029/2009GL039580> (2009).
30. Sun, Y., Niu, F., Chen, Y. & Liu, J. Crustal structure and deformation of the SE Tibetan plateau revealed by receiver function data. *Earth Planet. Sci. Lett.* **349**, 186–197 (2012).
31. He, C. S., Dong, S. W., Santosh, M. & Chen, X. H. Seismic evidence for a geosuture between the Yangtze and Cathaysia blocks, South China. *Sci. Rep.* **3**, 200. <https://doi.org/10.1038/srep02200> (2013).
32. Teng, J. et al. Investigation of the Moho discontinuity beneath the Chinese Mainland using deep seismic sounding profiles. *Tectonophysics* **609**, 202–216 (2013).
33. Reddy, P. R. & Rao, V. Seismic images of the continental Moho of the Indian shield. *Tectonophysics* **609**, 217–233 (2013).
34. Stankiewicz, J. & de Wit, M. 3.5 Billion years of reshaped Moho, Southern Africa. *Tectonophysics* **609**, 675–689 (2013).
35. Mjelde, R., Goncharov, A. & Müller, R. D. The Moho: boundary above upper mantle peridotites or lower crustal eclogites? A global review and new interpretations for passive margins. *Tectonophysics* **609**, 636–650 (2013).
36. Aitken, A. R. A., Salmon, M. L. & Kennett, B. L. N. Australia's Moho: A test of the usefulness of gravity modelling for the determination of Moho depth. *Tectonophysics* **609**, 468–479 (2013).
37. Grad, M., Tiira, T. & ESC Working Group. The Moho depth map of the European plate. *Geophys. J. Int.* **176** (1), 279–292 (2009).
38. Assumpção, M., Feng, M., Tassara, A. & Julià, J. Models of crustal thickness for South America from seismic refraction, receiver functions and surface wave tomography. *Tectonophysics* **609**, 82–96 (2013).
39. Tugume, F., Nyblade, A., Julià, J. & van der Meijde, M. Precambrian crustal structure in Africa and Arabia: evidence lacking for secular variation. *Tectonophysics* **609**, 250–266 (2013).
40. Nicolich, R. & Dal Piaz, G. Isobate Della Moho in Italia, in Structural Model of Italy, 6 Fogli 1:500,000, Progetto Finalizzato 'Geodinamica' CNR, Rome (1991).
41. Scarascia, S., Lozej, A. T. & Cassinis, R. Crustal structures of the Ligurian, tyrrhenian and ionian seas and adjacent onshore areas interpreted from wide-angle seismic profiles. *Bollettino Di Geofis. Teorica Ed. Appl.* **36** (141–44), 5–19 (1994).
42. Waldhauser, F., Kissling, E., Ansgor, J. & Müller, S. Three-dimensional interface modeling with two-dimensional seismic data: the alpine crust-mantle boundary. *Geophys. J. Int.* **135**, 264–278. <https://doi.org/10.1046/j.1365-246X.1998.00647.x> (1998).
43. Lippitsch, R., Kissling, E. & Ansgor, J. Upper mantle structure beneath the alpine orogen from high-resolution teleseismic tomography. *J. Geophys. Res.* **108** (B8), 2376. <https://doi.org/10.1029/2002JB002016> (2003).
44. Waldhauser, F. A parameterized three-dimensional Alpine crustal model and its application to teleseismic wavefront scattering. *Ph.D. Thesis Swiss Fed. Inst. Technol. Zurich Switzerland* (1996).
45. Pontevivo, A. & Panza, G. Group velocity tomography and regionalization in Italy and bordering areas. *Phys. Earth Planet. Inter.* **134**, 1–15. [https://doi.org/10.1016/S0031-9201\(2002\).0200079-1](https://doi.org/10.1016/S0031-9201(2002).0200079-1).
46. Lombardi, D., Braunmiller, J., Kissling, E. & Giardini, D. Moho depth and Poissons ratio in the Western central alps from receiver functions. *Geophys. J. Int.* **173**, 249–264. <https://doi.org/10.1111/j.1365-246X.2007.03706.x> (2008).
47. Piana Agostinetti, N. & Amato, A. Moho depth and Vp/Vs ratio in Peninsular Italy from teleseismic receiver functions. *J. Geophys. Res. Solid Earth* **114** (B6), (2009).
48. Di Stefano, R., Bianchi, I., Ciaccio, M. G., Carrara, G. & Kissling, E. Three-dimensional Moho topography in Italy: new constraints from receiver functions and controlled source seismology. *Geochem. Geophys. Geosyst.* **12** (9), (2011).
49. Spada, M., Bianchi, I., Kissling, E., Agostinetti, N. P. & Wiemer, S. Combining controlled-source seismology and receiver function information to derive 3-D Moho topography for Italy. *Geophys. J. Int.* **194** (2), 1050–1068 (2013).
50. Kherchouche, R., Ouyed, M., Aoudia, A., Mellouk, B. & Saadi, A. Structure of the crust and uppermost mantle beneath the Sicily channel from ambient noise and earthquake tomography. *Ann. Geophys.* **63** (6), SE666–SE666 (2020).
51. Jongsma, D., van Hinte, J. E. & Woodside, J. M. Geologic structure and neotectonics of the North African continental margin South of Sicily. *Mar. Pet. Geol.* **2** (2), 156–179. [https://doi.org/10.1016/0264-8172\(85\)90005-4](https://doi.org/10.1016/0264-8172(85)90005-4) (1985).
52. Corti, G., Cuffaro, M., Doglioni, C., Innocenti, F. & Manetti, P. Coexisting geodynamic processes in the Sicily channel. In postcollisional tectonics and magmatism in the mediterranean region and Asia. *Geol. Soc. Am.* [https://doi.org/10.1130/2006.2409\(05](https://doi.org/10.1130/2006.2409(05) (2006).
53. Scognamiglio, L., Tinti, E. & Quintiliani, M. Time domain moment tensor (TDMT) [Data set]. Istituto Nazionale di Geofisica e Vulcanologia (INGV). (2006).
54. Sulli, A., Morticelli, M. G., Agate, M. & Zizzo, E. Active north-vergent thrusting in the Northern Sicily continental margin in the frame of the quaternary evolution of the Sicilian collisional system. *Tectonophysics* **802**, 228717 (2021).
55. Cassinis, R., Scarascia, S., Lozej, A. & Finetti, I. R. Review of seismic wide-angle reflection–refraction (WARR) results in the Italian region (1956–1987). *CROP PROJECT Deep Seis. Explor. Cent. Mediterranean Italy* 31–55 (2005).
56. Agius, M. R. et al. Shear-velocity structure and dynamics beneath the sicily channel and surrounding regions of the central mediterranean inferred from seismic surface waves. *Geochem. Geophys. Geosyst.* **23** (10), eGC010394 (2022).
57. Finetti, I. R. Depth contour map discontinuity in the central mediterranean region from new CROP seismic data. *CROP PROJECT Deep Seis. Explor. Cent. Mediterranean Italy* 31–55 (2005).
58. Cavallaro, D., Monaco, C., Polonia, A., Sulli, A. & Di Stefano, A. Evidence of positive tectonic inversion in the North-Central sector of the Sicily channel (Central Mediterranean). *Nat. Hazards*. **86** (Suppl 2), 233–251. <https://doi.org/10.1007/s11069-016-2515-6> (2016).
59. Scholz, C. *The Mechanics of Earthquakes and Faulting* <https://doi.org/10.1017/9781316681473> (Cambridge University Press, 2019).
60. Watts, A. B. & Burov, E. B. Lithospheric strength and its relationship to the elastic and seismogenic layer thickness. *Earth Planet. Sci. Lett.* **213**, 113–131. [https://doi.org/10.1016/S0012-821X\(03\)00289-9](https://doi.org/10.1016/S0012-821X(03)00289-9) (2003).
61. Locardi, E. & Nicolich, R. Geodinamica Del Tirreno e Dell'Appennino centro-meridionale: La Nuova Carta Della Moho. *Memorie Della Società Geologica Italiana*. **41**, 121–140 (1988).
62. Spatola, D. et al. The Graham bank (Sicily channel, central mediterranean Sea): seafloor signatures of volcanic and tectonic controls. *Geomorphology* **318**, 375–389 (2018).
63. Viti, M., Albarello, D. & Mantovani, E. Rheological profiles in the central-eastern mediterranean. *Ann. Geofis.* **40** (4), (1997).
64. Maggi, A., Jackson, J., McKenzie, D. & Priestley, K. Earthquake focal depths, effective elastic thickness and the strength of the continental lithosphere. *Geology* **28**, 495–498 (2000).
65. Jackson, J. Strength of the continental lithosphere: time to abandon the jelly sandwich? *GSA Today*. **12**, 4–10 (2002).

66. Déverchère, J., Houdry, F., Diament, M., Solonenko, N. V. & Solonenko, A. V. Evidence for a seismogenic upper mantle and lower crust in the Baikal rift. *Geophys. Res. Lett.* **18** (6), 1099–1102 (1991).
67. Chen, W. & Yang, Z. Earthquakes beneath the Himalayas and Tibet: evidence for strong lithospheric mantle. *Science* **304**, 1949–1952 (2004).
68. Schulte-Pelkum, V., Monsalve, G., Sheehan, A., Pandey, M. & Sapkota, S. Bilham R. Imaging the Indian Subcontinent beneath the Himalaya. *Nature* **435**, 1222–1225 (2005).
69. Monsalve, G. et al. Seismicity and one-dimensional velocity structure of the Himalayan collision zone: earthquakes in the crust and upper mantle. *J. Geophys. Res. Solid Earth* **111** (B10) (2006).
70. Civile, D., Mangano, G., Micalfel, A., Lodolo, E. & Baradello, L. A failed rift in the Eastern adventure plateau (Sicilian channel, central Mediterranean). *J. Mar. Sci. Eng.* **12** (7), 1142 (2024).
71. Bindi, L., Tasselli, F., Olmi, F., Peccerillo, A. & Menchetti, S. Crystal chemistry of clinopyroxenes from Linosa volcano, Sicily channel, Italy: implications for modelling the magmatic plumbing system. *Mineral. Mag.* **66** (6), 953–968 (2002).
72. Vail, P. R. Seismic stratigraphy interpretation procedures. In *Atlas of Seismic Stratigraphy, AAPG Studies in Geology* Bally, A.W., Eds. **1** (27), 1–10 (1987).
73. Chironi, C. et al. Crustal structures of the Southern tyrrhenian sea and the Sicily channel on the basis of the M25, M26, M28, M39 WARR profiles. *Bollettino-Società Geologica Italiana*. **119** (1), 189–204 (2000).
74. Finetti, I. R. & Del Ben, A. Crustal tectono-stratigraphic setting of the Adriatic sea from new CROP seismic data. *CROP PROJECT: Deep Seismic Explor. Cent. Mediterranean Italy*. **1**, 519–548 (2005).
75. Menichelli, I. et al. Minimum 1D VP and VP/VS models and hypocentral determinations in the central mediterranean area. *Seismological Soc. Am.* **93** (5), 2670–2685 (2022).
76. Brocher, T. M. A regional view of urban sedimentary basins in Northern California based on oil industry compressional-wave velocity and density logs. *Bull. Seismol. Soc. Am.* **95** (6), 2093–2114. <https://doi.org/10.1785/0120050025> (2005).
77. ISIDe Working Group. ISIDe, Italian seismological instrumental and parametric database, version 1.0. <https://doi.org/10.13127/ISIDe> (2016).
78. Latorre, D., Di Stefano, R., Castello, B., Michele, M. & Chiaraluca, L. Catalogo delle Localizzazioni ASSolute (CLASS): locations (Version 1). Istituto Nazionale di Geofisica e Vulcanologia (INGV). <https://doi.org/10.13127/class.1.0> (2022).
79. Wiemer, S. & Wyss, M. Minimum magnitude of completeness in earthquake catalogs: examples from Alaska, the Western united States and Japan. *Bull. Seismol. Soc. Am.* **90** (4), 859–869 (2000).
80. Figlioli, A., Vitale, G., Taroni, M. & D'Alessandro, A. Tremors—A software app for the analysis of the completeness magnitude. *Geosciences* **14** (6), 149 (2024).
81. RStudio Team & Boston *Integrated Development for R. RStudio* <http://www.rstudio.com/> (PBC, 2020).
82. Scott, D. W. *Stima Della Densità Multivariata. Teoria, Pratica E Visualizzazione* (Wiley, 1992).
83. Hijmans, R. J. Raster: geographic data analysis and modeling, r package version 2.8-4 (2018).
84. Baddeley, A. & Turner, R. Spatstat: an R package for analyzing Spatial point patterns. *J. Stat. Softw.* **12**, 1–42 (2005).

## Acknowledgements

The authors would like to thank Salvatore Scudero (INGV-ONT) for the useful discussions and suggestions on this paper.

## Author contributions

S.B., M.M.: data analysis and interpretation of results, review of literature data, preparation of the figures, writing the main text of the manuscript; A.S.: interpretation of results, initial idea, work planning, review of the manuscript; R.M., A.D.: work planning, review of the manuscript.

## Declarations

### Competing interests

The authors declare no competing interests.

## Additional information

**Supplementary Information** The online version contains supplementary material available at <https://doi.org/10.1038/s41598-025-01189-7>.

**Correspondence** and requests for materials should be addressed to S.B.

**Reprints and permissions information** is available at [www.nature.com/reprints](http://www.nature.com/reprints).

**Publisher's note** Springer Nature remains neutral with regard to jurisdictional claims in published maps and institutional affiliations.

**Open Access** This article is licensed under a Creative Commons Attribution-NonCommercial-NoDerivatives 4.0 International License, which permits any non-commercial use, sharing, distribution and reproduction in any medium or format, as long as you give appropriate credit to the original author(s) and the source, provide a link to the Creative Commons licence, and indicate if you modified the licensed material. You do not have permission under this licence to share adapted material derived from this article or parts of it. The images or other third party material in this article are included in the article's Creative Commons licence, unless indicated otherwise in a credit line to the material. If material is not included in the article's Creative Commons licence and your intended use is not permitted by statutory regulation or exceeds the permitted use, you will need to obtain permission directly from the copyright holder. To view a copy of this licence, visit <http://creativecommons.org/licenses/by-nc-nd/4.0/>.

© The Author(s) 2025